D-Maurocalcine, a pharmacologically inert efficient cell-penetrating peptide analogue.

Cathy Poillot, Kaouthar Dridi, Hicham Bichraoui, Julien Pêcher, Sébastien Alphonse, Badreddine Douzi, Michel Ronjat, Hervé Darbon, Michel de Waard

▶ **To cite this version:**

Cathy Poillot, Kaouthar Dridi, Hicham Bichraoui, Julien Pêcher, Sébastien Alphonse, et al.. D-Maurocalcine, a pharmacologically inert efficient cell-penetrating peptide analogue.: Cell Penetrating D-Maurocalcine Peptide. Journal of Biological Chemistry, 2010, 285 (44), pp.34168-80. 10.1074/jbc.M110.104919 . inserm-00587800

HAL Id: inserm-00587800

https://inserm.hal.science/inserm-00587800

Submitted on 7 Jul 2011

HAL is a multi-disciplinary open access archive for the deposit and dissemination of scientific research documents, whether they are published or not. The documents may come from teaching and research institutions in France or abroad, or from public or private research centers.

L'archive ouverte pluridisciplinaire **HAL**, est destinée au dépôt et à la diffusion de documents scientifiques de niveau recherche, publiés ou non, émanant des établissements d'enseignement et de recherche français ou étrangers, des laboratoires publics ou privés.

D-MAUROCALCINE, A PHARMACOLOGICALLY-INERT EFFICIENT CELL PENETRATING PEPTIDE ANALOGUE

From Cathy Poillot[1,§] Kaouthar Dridi[2,§], Hicham Bichraoui[1], Julien Pêcher[3], Sebastien Alphonse[2], Badreddine Douzi[2], Michel Ronjat[1], Hervé Darbon[2], and Michel De Waard[1,3]

[1]Grenoble Institute of Neuroscience, Inserm U836, Site Santé de la Tronche, bâtiment Edmond J. Safra, Chemin Fortuné Ferrini, BP170, 38042 Grenoble Cedex 9, France ; [2]AFMB-CNRS - UMR 6098, Case 932 - 163 avenue de Luminy, F-13288 Marseille Cedex 9, France ; [3]Smartox Biotechnologies, Floralis, Biopolis, 5 Avenue du Grand Sablon, 38700 La Tronche, France.

Running head: Cell Penetrating D-Maurocalcine Peptide

Address correspondence to: Dr. Michel De Waard, GIN, Inserm U836, BP170, 38042 Grenoble, France. Phone: (33) 4 56 52 05 63 - Fax: (33) 4 56 52 06 37 - E-mail: michel.dewaard@ujf-grenoble.fr

[§]Both authors contributed equally to this work.

Maurocalcine has been the first demonstrated animal toxin acting as a cell penetrating peptide. Although it possesses competitive advantages, its use as cell penetrating peptide (CPP) requires that analogues have to be developed that lack its characteristic pharmacological activity on ryanodine-sensitive calcium channels without affecting its cell penetrating and vector efficiencies. Here, we present the synthesis, 3-D ^{1}H-Nuclear Magnetic Resonance (^{1}H-NMR) structure and activity of D-maurocalcine. We demonstrate that it possesses all the desired features for an excellent cell penetrating peptide: preserved structure, lack of pharmacological action, conserved vector properties, and absence of cell toxicity. This is the first report of a folded/oxidized animal toxin in its D-diastereomer conformation for use as CPP. The protease resistance of this new peptide analogue, combined with its efficient cell penetration at concentrations devoid of cell toxicity, suggests that D-maurocalcine should be an excellent vector for *in vivo* applications.

Over the last 15 years, several peptides have been described as possessing the property to accumulate inside cells. These peptides have collectively been denominated Cell Penetrating Peptides (CPP) (1). The common characteristic of these peptides is that they are unusually enriched in positively-charged amino acids (2). The HIV-1 TAT peptide, penetratin and the chimeric transportan are well-known and frequently used CPP (3,4). Reports on the use of CPP as vectors for the cell delivery of non-permeable membrane compounds are now blossoming. As a consequence, many novel applications have been developed that are based on the cell delivery of drugs, peptides, proteins, antibodies, oligonucleotides, peptide nucleic acids, siRNA, cDNA, imaging agents or nanoparticles (5-7). The mechanism(s) by which CPP enter cells remains largely debated, but the consensual view is that two non-concurrent pathways coexist: direct membrane translocation and one of many forms of endocytosis (8). This discussion is not only semantic since the intracellular distribution and fate of CPP differs with its mode of entry. If direct translocation is used, the peptide accumulates in the cytoplasm and reaches the nucleus, while, if endocytosis is the main pathway of cell entry, peptides end up in late endosomes. Translocation is the favored pathway for the cell delivery of cargoes by CPP since most drugs are active when delivered in the cytoplasm or in the nucleus, but not in late endosomes (4,9).

While searching for pharmacological agents regulating the activity of ryanodine receptors (RyR), our group came across a cationic toxin of 33-mer, maurocalcine (L-MCa), which was originally isolated and purified from a Tunisian scorpion, *Scorpio maurus palmatus* (10). RyR are intracellular calcium channels that are inserted into the membrane of endoplasmic reticulum and that control Ca^{2+} release from intracellular stores. Several lines of evidence suggested that L-MCa represents the first member of a novel class of CPP. Firstly, it was demonstrated that an extracellular application of

L-MCa triggers an almost immediate Ca^{2+} release from internal stores in myotubes suggesting rapid access of L-MCa to its binding site (11). Secondly, it was discovered that L-MCa's binding site is located on the cytoplasmic side of RyR (12). Kinetic and RyR topological considerations therefore suggest that cell entry of L-MCa more likely relies on membrane translocation to achieve rapid cytoplasmic accumulation than on endocytosis. Thirdly, L-MCa acts as an efficient vector for the delivery of proteins, peptides, nanoparticles and drugs inside cells. At the structural level, the peptide folds along an inhibitor cystine knot motif with three disulfide bridges connected according to the pattern Cys^{3}-Cys^{17}, Cys^{10}-Cys^{21}, and Cys^{16}-Cys^{32}. Landmark properties of CPP are also found in L-MCa since (i) 12 out of the 33 residues of L-MCa are positively charged, (ii) many of the charged residues are critical for cell penetration, and (iii) L-MCa interacts with critical membrane components required for cell penetration such as proteoglycans and negatively charged lipids (13,14). Altogether, these considerations made L-MCa the first example of a folded and oxidized peptide toxin acting as CPP. Compared to other CPP, it possesses some competitive features such as greater stability, cell penetration at lower concentrations, very low toxicity and membrane translocation as expected mode of cell penetration. Besides it is one of the few CPP whose cell penetration can be studied independently of cargo attachment since it possesses a direct physiological readout under the form of Ca^{2+} release from internal stores. Two negative aspects related to the use of L-MCa instead of other CPPs are (i) longer length of the peptide and (ii) pharmacological activity associated to cell penetration. Peptide length has little economical impact now since the cost of peptide production has sharply decreased. In contrast, pharmacological activity may represent a burden if one wants to use L-MCa as vector for its application *in vivo*. To circumvent this problem, several strategies have been developed based on the assumption that the structural requirements for binding onto RyR were more stringent than those for cell penetration. First, single point mutagenesis of L-MCa was employed in order to alter peptide pharmacology without affecting cell penetration. Using this strategy, new L-MCa analogues have been defined with reduced or complete loss of pharmacological effects (13). Nevertheless, none of the analogues totally preserved the cell penetration efficiency of wild-type L-MCa. Second, an L-MCa analogue was produced in which all cysteine residues were substituted with isosteric 2-aminobutyric acid residues (15). The resulting peptide was unfolded owing to the importance of disulfide bridges for folding/oxidation and lacked pharmacological properties. Interestingly, this analogue preserved correct cell penetration efficacy, albeit lower than L-MCa. In addition, lack of secondary structures and absence of disulfide bridges result in the loss of the competitive advantage of MCa over other CPP. Herein, we pursued another strategy with the aim to produce a cell-penetrating competent MCa analogue, similar in properties to L-MCa, but without any pharmacological activity. We describe the chemical synthesis, successful folding and oxidation of D-MCa, provide the 3-D structure of the resulting analogue and demonstrate that it has similar cell penetration properties than L-MCa. In addition, D-MCa loses the protease-sensitivity of L-MCa and is a non toxic vector for cells. This is the first description of a folded/oxidized CPP build with D-amino-acids and designed on the basis of an animal toxin sequence.

Experimental Procedures

Materials and methods - N-α-Fmoc-L-aminoacid, N-α-Fmoc-D-aminoacid, Wang-Tentagel resin and reagents used for peptide synthesis were obtained from Iris Biotech. Solvent were analytical grade products from Acros Organics. Enzymes (trypsin, endoproteinase Asp-N) were obtained from Roche.

General procedures: solid-phase synthesis - The chemical synthesis of L-MCa was performed as previously described (10). D-MCa was chemically synthesized by the solid-phase method (16) using an automated peptide synthesizer (CEM© Liberty). Peptide chain was assembled stepwise on 0.24 mEq of Fmoc-D-Arg-Pbf-Wang-Tentagel resin using 0.24 mmol of N-α-fluorenylmethyloxycarbonyl (Fmoc) D-amino-acid derivatives. The side-chain protecting groups were: Trityl for Cys and Asn, *tert*-butyl for Ser, Thr, Glu and Asp, Pbf for Arg and *tert*-

butylcarbonyl for Lys. Reagents were at the following concentrations: Fmoc-amino-acids (0.2 M Fmoc-AA-OH in dimethylformamide (DMF)), activator (0.5 M HBTU in DMF), activator base (2 M DIPEA in N-methyl-pyrrolidone (NMP)) and deprotection agent (5% piperazine / 0.1 M HOBt in DMF), as advised by PepDriver (CEM©). After peptide chain assembly, the resin was treated 4 hrs at room temperature with a mixture of trifluoroacetic acid/water/triisopropylsilan (TIS)/dithiothreitol (DTT) (92.5/2.5/2.5/2.5). The peptide mixture was then filtered, and the filtrate was precipitated by adding cold *t*-butylmethyl ether. The crude peptide was pelleted by centrifugation (10.000 × g, 15 min) and the supernatant was discarded. The reduced peptide was dissolved in 200 mM Tris-HCl buffer, pH 8.3, at a final concentration of 1 mM and stirred 72 hrs at room temperature under air for oxidation and folding. Oxidized D-MCa was purified by HPLC using a Vydac C18 column (218TP1010, 25×10 cm). Elution of D-MCa was performed with a 10-60% acetonitrile linear gradient containing 0.1% trifluoroacetic acid. The purified fraction was analyzed by analytical RP-HPLC (Vydac C18 column 218TP104, 25 × 4.6 cm). The pure fraction lyophilized and quantified. 25 mg of D-MCa was purified, representing a theoretical yield of 25%. D-MCa was characterized by MALDI-TOF mass spectrometry.

D-MCa labeling by FAM – The carboxyl function of 5(6)-Carboxyfluorescein (0.25 mmol, Novabiochem) was activated in 1 ml solution of 1 M N,N'-diisopropylcarbodiimide (DICC, Sigma) /1 M HOBt in NMP for 30 min. This solution was then added to 100 mg (0.012 mmol) of D-MCa lateral chain-protected linked to the Wang-Tentagel resin. The reaction mixture was stirred for 2.5 hrs in the dark, and then centrifuged. The resin was washed with NMP five times, followed by three washes with methanol. The final resin was dried, and subjected 4 hrs at room temperature to peptide cleavage with a mixture of trifluoroacetic acid/water/triisopropylsilan (TIS)/dithiothreitol (DTT) (92.5/2.5/2.5/2.5). Next, crude FAM-D-MCa was oxidized as described for D-MCa.

Proteolytic digestion of L-MCa and D-MCa - The stability of D-MCa to proteolytic digestion was investigated under the same conditions used to determine the disulfide bridge of L-MCa toxin. D-MCa (400 µg) was dissolved in 50 mM sodium phosphate buffer and Endoproteinase Asp-N (enzyme/substrate, 1/200, w/w, 37°C, 36 hrs) or trypsin (enzyme/substrate, 1/32, w/w, 37°C, 36 hrs). The digestion was terminated by acidification with 10% aqueous TFA. The product was analyzed directly by RP-HPLC with a linear gradient of 1 to 60% acetonitrile into water containing 0.1% trifluoroacetic acid.

Circular dichroism - The folding states of L- and D-MCa were checked by far-UV circular dichroism (CD). The CD spectra were recorded on a Jasco 810 dichrograph using 1 mm thick quartz cells in 300 µl water. CD measurements were performed at 298 K, using a wavelength ranging from 260 to 190 nm. Peptide concentrations were 0.1 mM for these measurements. D-MCa thermal stability was assessed using CD by following changes in the spectrum with increasing temperature at fixed wavelength (200 nm). Measurements were performed in the temperature range of 20°C - 100°C with data pitch of 10°C step and temperature rise of 5°C/min.

NMR experiments - Purified D-MCa was solubilized in 500 µl of a mixture of H_2O and D_2O (9/1, v/v) at a final concentration of 1.9 mM. Amide proton exchange rates were determined after freeze-drying of the sample and solubilization in 100% D_2O. All ^{1}H-NMR spectra were recorded on a Bruker DRX500 Avanced III spectrometer equipped with a QX1 probe with Z axis gradients. The temperature was set to 300 K and the spectra were recorded with 2048 complex points in the directly acquired dimension and 400 points in the indirectly detected dimension (4,096 × 512 points for the DQF-COSY). Solvent suppression was achieved using excitations sculpting with gradients (17). Two-dimensional spectra were acquired using states-TPPI method (18) to achieve F1 quadrature detection (19). NOESY spectra were acquired using a mixing time of 100 ms. TOCSY was performed with a spin locking field strength of 8 kHz for 80 ms. The individual amide proton exchange rates were determined by recording series of six NOESY spectra (10 hrs duration for each experiment) at 300 K using the D_2O sample. Amide proton exchange still giving rise to nuclear Overhauser effect (nOe) correlations after 60 hrs of exchange

were considered as slowly exchanging and therefore engaged in a hydrogen bond, the partner of which being identified on the sight of preliminary calculated structures. All spectra were processed with NMRPipe (20).

Spectrum analysis and experimental restraints - The identification of amino-acid spin systems and the sequential assignment were done using standard strategy described by Wüthrich (21), applied with NMRview 5.2 graphic software (22). The comparative analysis of COSY and TOCSY spectra recorded in water gave the spin system signatures of the peptide. The spin systems were then sequentially connected using NOESY spectra. The integration of nOe data was performed by measuring peak volumes. On the basis of known distances in regular secondary structures, these volumes were translated into upper limit distances with CYANA 2.1 (23). Remaining nOe were assigned using the CANDID/NOEASSIGN automatic procedure of CYANA 2.1. Chemical shifts have been deposited to the BMRB Data Bank with Accession Number 16605. The calculation, after modification of libraries to integrate D-amino-acid configuration, consisted of seven cycles of iterative automated nOe assignment and structure calculation of 250 conformers in each cycle. At the end of each CYANA run, unambiguously assigned peaks were converted in distance restraints and used as inputs for the next calculation steps. To keep the similar assignment condition, the same nOe calibration parameter, calculated by CYANA during the first run of nOe assignment, was used in all other runs of calculation. The final structure calculations with CYANA were started from 600 conformers and a simulated annealing with 20,000 time steps per conformer was done using the CYANA torsion angle dynamics algorithm (24,25). The 100 best solutions were refined using a short restrained molecular dynamics simulation in explicit solvent (26,27) in the program XPLOR-NIH (28). At the end of the refinement, the 20 lowest energy solutions were selected to form the final ensemble. The quality of the structure was analyzed with PROCHECK-NMR (29) and WHATIF (30) programs. Superposition of the structures was performed using the McLachlan algorithm as implemented in the program ProFit (Martin, A.C.R., http://www.bioinf.org.uk/software/profit/). All structure representations were made with the program PYMOL (DeLano Scientific, Palo Alto, CA, USA. http://www.pymol.org). The atomic coordinates and experimentally derived restraints have been deposited in the Protein Data Bank with Accession Number 2KQL.

Preparation of heavy SR vesicles - Heavy SR vesicles were prepared following the method of Kim et al. (31). Protein concentration was measured by the Biuret method.

[^{3}H]-Ryanodine binding assay - Heavy SR vesicles (1 mg/ml) were incubated at 37°C for 2 hrs in an assay buffer composed of 10 nM [^{3}H]-ryanodine, 150 mM KCl, 2 mM EGTA, 2 mM $CaCl_2$ (*p*Ca = 5), and 20 mM MOPS, pH 7.4. L-MCa or D-MCa was added prior to the addition of heavy SR vesicles. [^{3}H]-ryanodine bound to heavy SR vesicles was measured by filtration through Whatman GF/B glass filters followed by three washes with 5 ml of ice-cold washing buffer composed of 150 mM NaCl, 20 mM HEPES, pH 7.4. [^{3}H]-ryanodine retained on the filters was measured by liquid scintillation. Non-specific binding was measured in the presence of 80 µM unlabeled ryanodine. The data are presented as mean ± S.E. Each experiment was performed in triplicate.

Ca^{2+} release measurements - Ca^{2+} release from heavy SR vesicles was measured using the Ca^{2+}-sensitive dye antipyrylazo III. The absorbance was monitored at 710 nm by a diode array spectrophotometer (MOS-200 optical system, Biologic, Claix, France). Heavy SR vesicles (50 µg) were actively loaded with Ca^{2+} at 37°C in 2 ml of a buffer containing 100 mM KCl, 7.5 mM sodium pyrophosphate, 20 mM MOPS, pH 7.0, supplemented with 250 µM antipyrylazo III, 1 mM ATP/$MgCl_2$, 5 mM phosphocreatine, and 12 µg/ml creatine phosphokinase (25). Ca^{2+} loading was started by sequential additions of 50 and 20 µM $CaCl_2$. In these loading conditions, no calcium-induced calcium release interfered with the observations. At the end of each experiment, Ca^{2+} remaining in the vesicles was determined by the addition of 4 µM Ca^{2+} ionophore A23187 (Sigma), and the absorbance signal was calibrated by two consecutive additions of 20 µM $CaCl_2$.

Cell culture - Chinese hamster ovary (CHO) cell line (from ATCC) were maintained at 37°C in 5% CO_2 in F-12K nutrient medium (InVitrogen) supplemented with 10% (v/v) heat-inactivated

fetal bovine serum (InVitrogen) and 10,000 units/ml streptomycine and penicillin (InVitrogen).

MTT assay - Cells were seeded into 96-well micro plates at a density of approximately 8×10^4 cells/well. After 2 days of culture, the cells were incubated for 24 hrs at 37°C with L-MCa or D-MCa at a concentration of 10 µM. Control wells containing cell culture medium alone or with cells, both without peptide addition, were included in each experiment. 0.1% saponin was used as toxic agent for comparison. The cells were then incubated with 3-(4, 5-dimethylthiazol-2-yl)-2, 5-diphenyl-tetrazolium bromide (MTT) for 30 min. Conversion of MTT into purple colored MTT formazan by the living cells indicates the extent of cell viability. The crystals were dissolved with dimethyl sulfoxide (DMSO) and the optical density was measured at 540 nm using a microplate reader (Biotek ELx-800, Mandel Scientific Inc.) for quantification of cell viability. All assays were run in triplicates.

Confocal microscopy - For analysis of the subcellular localization of FAM-L-MCa or FAM-D-MCa in living cells, cells were incubated with the fluorescent peptides for 2 hrs, and then washed with phosphate-buffered saline (PBS) alone. The plasma membrane was stained with 5 µg/ml rhodamine-conjugated concanavalin A (Molecular Probes) for 5 min. Cells were washed once more. Live cells were then immediately analyzed by confocal laser scanning microscopy using a Leica TCS-SPE operating system. Rhodamine (580 nm) and FAM (517 nm) were sequentially excited and emission fluorescence were collected in z-confocal planes of 10–15 nm steps. In some experiments, FAM-D-MCa incubation with CHO cells coincided with a 20 min incubation with 50 nM LysoTracker red DND-99 before confocal acquisition.

FACS – FAM-L-MCa or FAM-D-MCa were incubated 2 hrs with CHO cells to allow cell penetration. The cells were then washed twice with PBS to remove excess extracellular peptide. Next, the cells were treated with 1 mg/ml trypsin (Invitrogen) for 10 min at 37°C to detach cells from the surface, and centrifuged at 500 *g* before suspension in PBS. For experiments concerning endocytosis inhibitors, CHO cells were initially washed with F12K and preincubated for 30 min at 37°C with different inhibitors of endocytosis: (i) 1 mM amiloride, (ii) 5 µM cytochalasin D, (iii) 5 mM nocodazole, or (iv) 5 mM methyl-β-cyclodextrin (all from Sigma). The cells were then incubated for 2 hrs at 37°C with 1 µM FAM-D-MCa. For all these experimental conditions, flow cytometry analyses were performed with live cells using a Becton Dickinson FACS LSR II flow cytometer (BD Biosciences). Data were obtained and analyzed using FCS express software (De Novo). Live cells were gated by forward/side scattering from a total of 50,000 events.

Statistical analyses - All data are given as mean ± SD for n number of observations, and statistical significance (p) was calculated using Student's t test.

RESULTS

Chemical Synthesis of D-MCa and Enzymatic Stability. The amino acid sequence and the expected disulfide bridge organization of D-MCa are illustrated in Figure 1A. Solid-phase chemical synthesis of D-MCa was achieved stepwise on 0.1 mmol of Fmoc-D-Arg-(2,2,4,6,7-pentamethyldihydrobenzofuran-5-sulfonyl (Pbf))-Wang-Tentagel resin by means of an Fmoc strategy. The amount of target peptide linked to the resin was 0.085 mmol indicating an 85% yield of peptide assembly. Indeed, a relative homogeneity of crude D-MCa was obtained after trifluoroacetic acid (TFA) treatment as witnessed by analytical C_{18} reversed phase high-performance liquid chromatography (HPLC) (Figure 1B). Crude D-MCa was then folded/oxidized for 72 hrs in alkaline conditions, and the main peptide purified to >99% homogeneity by semi-preparative C18 reversed-phase HPLC. The purity of D-MCa is illustrated by analytical C_{18} reversed phase HPLC and the folding/oxidation process witnessed by the shift in elution time (Figure 1B). MS analyses (MALDI-TOF technique) of crude and folded/oxidized D-MCa provide experimental molecular masses $(M+H)^+$ of 3866.5 and 3860.4 Da, respectively. The shift in experimental molecular mass of 6.1 Da upon folding/oxidation is in agreement with the engagement of all six cysteine residues in the formation of three disulfide bridges. The yield of D-MCa synthesis, following peptide assembly, TFA treatment, oxidative folding and purification was 25%. The enzymatic susceptibility of D-MCa

was determined by *in vitro* incubation of D-MCa with either trypsin or endoproteinase Asp-N (Figure 1C). As shown by analytical C_{18} reversed phase HPLC, D-MCa was totally resistant to the action of these enzymes while L-MCa was significantly degraded. This is a significant advantage of D-MCa over L-MCa if *in vivo* applications are pursued with these CPP.

CD analysis and Thermal Stability of D-MCa. The circular dichroism (CD) spectrum of D-MCa was determined to assess its secondary structure, and compared to the CD spectrum of L-MCa (Figure 2A). Measurements were performed at wavelengths ranging from 260 nm to 190 nm. The far-UV spectrum of D-MCa show essentially π-π^* transitions of the amide chromophore of the peptide backbone and a large positive contribution between 200 and 210 nm, indicating the presence of β-strand structures which is coherent with the structure of L-MCa (32). Interestingly, the CD spectrum of D-MCa is a mirror image of the one recorded for L-MCa revealing the persistence of the conformation and the presence of alpha carbons in D-configuration. The presence of disulfide bridges in D-MCa should represent a competitive advantage over other CPP in terms of peptide stability. To assess this point, the CD spectra of D-MCa was recorded at several different temperatures (20°C, 40°C, 60°C, 80°C and 100°C). All CD spectra coincided well indicating that the structure of D-MCa was remarkably stable with increasing temperatures (Figure 2B). A thermal denaturation/renaturation cycle has been performed on D-MCa from 20°C to 100°C by following the ellipticity value at 200 nm. This value remains constant within the temperature range demonstrating that D-MCa structure is resistant to thermal denaturation (Figure 2C).

Determination of the 3-D solution structure of D-MCa. NMR resonance assignment and structure calculation were performed for D-MCa. The spin systems were identified on the basis of both COSY and TOCSY spectra. Once assignment procedure was achieved, almost all protons were identified and their resonance frequency determined (Table 1). The 3D structure was determined by using 390 nuclear Overhauser effect (nOe)-based distance restraints (including 158 intra-residue restraints, 116 sequential restraints, 36 medium-range restraints, and 80 long-range restraints). The distribution of these nOe-based distance restraints along the sequence is shown in Figure 3A. In addition, 12 hydrogen bond restraints derived from hydrogen-deuterium exchange data have been included, as well as 9 distance restraints derived from the three disulfide bridges (Cys^3-Cys^{17}, Cys^{10}-Cys^{21}, Cys^{16}-Cys^{32}) as previously determined for L-MCa (32). Altogether, the final experimental set corresponds to 11.81 constraints per residue on the average. The final step of calculation including the whole set of restraints (see Table 2) led to 900 solutions from which the 100 best were energy-minimized in explicit solvent. The 20 best solutions (no residual violation greater than 0.1 Å) were kept for analysis (Figure 3B). The root mean square deviation (rmsd) calculated on the ensemble, excluding C- and N-terminal residues is 1.1 ± 0.2 Å for backbone atoms and 2.32 ± 0.24 Å if all non-hydrogen atoms are included (Figure 3A and Table 2). If only the ordered regions (amino-acids 8-10, 20-23, 30-32) are considered, these rmsd values drop to 0.43 ± 0.08 Å and 1.37± 0.19 Å, respectively. These values indicate a lower resolution for the unordered regions (Figure 3B). This is confirmed by the individual rmsd values and by the scarcity of constraints in these regions (Figure 3A). The correlation with the experimental data shows no nOe-derived distance violation greater than 0.1 and the Ramachandran plot, after modification of the library to include D-amino-acid configurations, shows (in PROCHECK software nomenclature) 95.5% of the residues in the allowed regions and 0.5% in the disallowed regions.

The three-dimensional conformation of D-MCa (PDB accession code: 2KQL) consists of a compact disulfide-bonded core, from which several loops and the N-terminus emerge. The main element of regular secondary structure is a double-stranded anti-parallel β-sheet comprising residues 20-23 and 30-32. A third peripheral extended strand composed by residues 8 to 10 is almost perpendicular to the double-stranded anti-parallel β-sheet (Figure 3C). MCa is the first scorpion toxin known to adopt an ICK motif while this fold has been observed for several other animal toxins from spider and shell venoms (33). To compare the native structure with the D-configuration herein described, we recalculated the L-configuration by using the previously

published NMR data set (32) with the same protocol as for the D-configuration (Figure 3C). This newly calculated structure of L-MCa is pretty close to the previously published one (rmsd: 0.51 Å on the ordered regions) (32). To objectively compare the L- and D-MCa three dimensional structures, we modified the pdb file of D-MCa in order to draw the peptide in the L-configuration. The superimposition of both structures is shown in Figure 4. rmsd values between both structures is 1.18 Å for backbone atoms (this value drops to 0.44 on ordered structures) and 2.07 Å for all non-hydrogen atoms. Therefore, the molecule, synthesised in D-configuration for alpha carbons adopts a fold which is a pure mirror image of the L-configuration (Figure 3C). This inversion is also seen on the organization of the molecular surface, leading to (i) the conservation of the basic patch and of the overall electrostatic anisotropy (the resulting dipole moment is conserved both in direction and strength) and (ii) the geometry inversion of the toxin surface involved in interaction with RyR (not shown). The conservation of the basic patch implies that membrane translocation properties should be well conserved, whereas geometry inversion of toxin surface should affect the ability of D-MCa to recognize RyR.

D-MCa is a pharmacologically inert analogue of L-MCa. D-isomer ligands are supposed to lose their ability to recognize their pharmacological targets. L-MCa is known to bind onto a discrete binding site of RyR (12) thereby triggering an increase in channel opening probability and the occurrence of a long-lasting sub-conductance state (34). Also, channel opening by L-MCa can indirectly be monitored by the conversion of a low affinity binding site for ryanodine to a high affinity one (11), and by Ca^{2+} release from purified sarcoplasmic reticulum (SR) vesicles (35). We therefore investigated the effects of D-MCa on these two paradigms (Figure 5). As shown, L-MCa potently increases [^{3}H]-ryanodine binding on heavy SR vesicles known to contain RyR. Maximal binding stimulation is 6.2-fold and occurs with an EC_{50} of 17.8 nM. In contrast to L-MCa, D-MCa had no effect on [^{3}H]-ryanodine binding and this for concentrations up to 1 µM (Figure 5A). We have repeatedly illustrated that L-MCa triggers Ca^{2+} release from purified heavy SR vesicles (11,35,36). Under similar experimental conditions, heavy SR vesicles, initially loaded with Ca^{2+}, did not respond to an extra-vesicular application of 1 µM D-MCa. In contrast, when this application was followed by an application of a much lower concentration of L-MCa (60 nM), a massive Ca^{2+} release was observed (Figure 5B). Altogether, these data argue that D-MCa, while being a mirror structure of L-MCa, is totally pharmacologically inert with regard to RyR channel activation.

Labeling of D-MCa by FAM and cell penetration properties. To investigate the cell penetration properties of D-MCa, it was first covalently coupled to 5(6)-carboxyfluorescein (FAM) using a peptide bond at the N-terminus of the peptide (Figure 6A). FAM is represented here by two isomers that may differ slightly in hydrophobicity during HPLC purification. After synthesis, FAM-D-MCa was purified by reverse-phase C18 HPLC. As shown, the purified folded/oxidized FAM-D-MCa differs significantly of D-MCa in elution time suggesting that the resulting cargo-vector chimera was more hydrophobic than the vector itself (Figure 6B). MS analysis of pure folded/oxidized FAM-D-MCa provides an experimental molecular mass $(M+H)^+$ of 4215.8 Da confirming the correct assembly of the cargo-vector chimera molecule (inset Figure 6B). Next, we investigated whether FAM-D-MCa could penetrate into live CHO cells. 1 µM FAM-D-MCa was incubated for 2 hrs with live CHO cells, labeled for plasma membrane with concanavalin-A-rhodamin, and examined immediately by confocal microscopy. As shown, FAM-D-MCa was present in all cells but the distribution was variable from cell to cell (Figure 6C). This distribution was fully comparable to the distribution observed for FAM-L-MCa, synthesized according to the same principles than FAM-D-MCa (synthesis not described herein). These data indicate that D-MCa preserves the cell penetration properties of L-MCa. Confocal images further suggest that the labeling of D-MCa-FAM is intracellular rather than membranous. To reinforce this observation, we analyzed how much of the D-MCa-FAM colocalized with the plasma membrane staining (Figure 6D). As shown, a very small fraction of the D-MCa-FAM was colocalized with

concanavalin A-rhodamin staining (6.2% of total FAM-colored pixels).

In many cells, D-MCa-FAM penetration results in a mixed distribution (cytoplasm in addition to a punctuate distribution). These coincident distributions have been interpreted as evidence that two mechanisms of cell penetration of FAM-D-MCa coexist: translocation for cytoplasm distribution and a form of endocytosis for endosomal punctuate distribution, as evidenced in earlier studies (14,15,37). The use of any one of these two entry pathways is possibly under the influence of the nature and size of the cargo. Therefore, we reinvestigated the nature of FAM-D-MCa cell entry by using various inhibitors of the endocytosis route (Figure 7). LysoTracker red stains endosomal structures. As shown, 73.5% of endosomal structures were also positive for FAM-D-MCa (Figure 7A,B). In addition, a significant fraction of FAM-D-MCa staining (55.4%) was endosome-negative, suggesting the coexistence of two types of cell distributions (more than half not related to endosomes, and less than half endosomal). These ratio between both distributions differ from the one observed using fluorescent streptavidine as cargo. With streptavidine, we have shown that the macropinocytosis inhibitor, amiloride, blocks 80% of cell entry (14). Here, we quantified by fluorescence-activated cell sorting (FACS) the effects of nocodazole (microtubule formation inhibitor), cytochalasin D (F-actin elongation inhibitor), methyl-β-cyclodextrin (lipid raft-dependent endocytosis inhibitor by cholesterol depletion) and amiloride (macropinocytosis inhibitor) on the cell penetration of FAM-D-MCa. As expected if endocytosis is involved in cell penetration of FAM-D-MCa, disturbing the microtubule or actin filament system with nocodazole or cytochalasin D induces a 50.5 ± 19.8% or 59.3 ± 13.4% inhibition of cell entry (Figure 7C,D). Amiloride inhibited cell entry of FAM-D-MCa by 53.4 ± 22%, which is less than when streptavidine is used as cargo. Interestingly, methyl-β-cyclodextrine, which inhibits lipid raft-dependent endocytosis, also inhibits mildly the cell penetration of FAM-D-MCa (by 15.8 ± 27%), which was not observed for streptavidine as cargo (14). This result indicates that macropinocytosis remains the major mode of FAM-D-MCa cell penetration by endocytosis. It also informs that the nature of cargo influences to what extent endocytosis is used over cell translocation for cell penetration. In particular, with a small cargo such as FAM, a significant fraction of the peptide is susceptible to enter through membrane translocation even if endocytosis is a major route of cell entry.

D-MCa is a non-toxic cell penetrating peptide of similar efficacy than L-MCa. Using FACS we also compared the dose-response curve of the cell entry of FAM-D-MCa with that of FAM-L-MCa. CHO cells were incubated with various concentrations of FAM-D-MCa for two hours, cells treated with trypsin for plastic support detachment, and immediately evaluated for fluorescence intensity by FACS. As shown, the cell penetration of FAM-D-MCa is dose-dependent with a positive signal starting at 100 nM and signals still increasing at a concentration of 3.3 μM (Figure 8A). The dose-dependent cell penetration of FAM-L-MCa was identical to that of FAM-D-MCa at all concentrations tested (Figure 8B). The average fluorescence of each CPP-cargo complex was plotted as a function of concentration (Figure 8C). As shown, FAM-D-MCa penetrates with the same dose-dependence than FAM-L-MCa. Concentrations required for half-maximal cell penetration were 1.38 μM and 1.78 μM for FAM-D-MCa and FAM-L-MCa, respectively. Finally, a good CPP is also one that presents no cell toxicity. Both D-MCa and L-MCa were evaluated for their toxic effects by incubation with CHO cells for 24 hours. As shown, both peptides had no toxic effects at concentrations of 10 μM, contrary to 0.1% saponin (Figure 8D).

DISCUSSION

MCa is one additional member of the exponentially growing list of reported CPP. It is however one of the rare CPP that is fully natural and that presents such a well-defined 3D structure. However, because of its intrinsic pharmacological properties, it requires the design of new analogues that take advantage of its peculiar cell penetrating efficacy without the drawback of its activity. One design strategy, based on the replacement of cysteine residues by 2-aminobutyric acid residues and the consequent loss of secondary structure, led to the successful

production of a pharmacologically-inert but potent cell penetrating MCa analogue. This strategy however eliminated some of the MCa features that distinguish it from other classical CPP. In particular, this analogue is no longer folded and it loses some of its cell penetrating efficacy. The present strategy, consisting to successfully produce D-MCa, was aimed to circumvent both of these drawbacks. In addition, the use of D-amino acids renders the peptide resistant to protease action, making it a particularly useful vector for *in vivo* applications. While several natural toxin/peptides are known to contain D-amino acids, such as several conopeptides (38-40), none have a primary structure based on the sole use of D-amino acids. The presence of such amino acids in the sequence has been linked to toxin activity. In r11a, a 46-amino acid I_1-conotoxin (41), has a phenylalanine at position 44 which undergoes epimerization from an L-Phe to a D-Phe, a transition linked to a dramatic gain in pharmacological activity (39). Similarly, isomerisation of L-Phe to D-Phe also enhanced biological activity of conomap-Vt, a linear peptide from *Conus vitulinus* (40). The complete chemical synthesis of a toxin with only D-amino acids has been seldom reported. In one pioneering work, Di Luccio and collaborators reported the chemical synthesis of D-maurotoxin, a four-disulfide-bridged toxin active on potassium channels (42). Interestingly, the kinetic features of the *in vitro* oxidation/folding of D-maurotoxin are indistinguishable from those of L-maurotoxin. In contrast, the effects of PDI (that catalyses breakage and re-formation of disulfide bridges) and PPIase (that controls isomerisation between the cis and trans configurations of prolyl imidic peptide bonds) on *in vitro* oxidation/folding of maurotoxin were stereo-selective. In another example, the 35 amino acid residue sea anemone ShK toxin that blocks potassium channels was also synthesized with amino acids that have a D-configuration at alpha carbon (43). This peptide also folded as a mirror image of L-ShK. Curiously, pharmacological experiments and docking simulation analyses indicate that D-ShK has the ability to recognize and block $K_v1.3$ channels, albeit with a reduced affinity. This may occur because of the fourfold symmetry of $K_v1.3$ channels and because of the compact set of interactions taking place (Lys^{22} filling in the ion selectivity filter, and Arg^{24} and Arg^{29} interacting with His^{404} of the channel). In another example of a violation of the traditional lock-and-key model of ligand-target interaction, it was found that the D enantiomer of GsMTx4, a peptide of the venom of tarantula *Grammostola spatulata*, remained active on stretch-activated cation channels (44). This effect is proposed to occur through local bilayer thinning without requiring a physical contact with the channel. In the case of MCa, we found that producing this CPP with D-amino acids does also not interfere with its folding and with the correct formation of disulfide bridges. The disulfide bridge pattern could not be assessed as usual, i.e. by limited trypsin digestion of the folded/oxidized peptide followed by MS analyses. In contrast, we confirmed the correct folding and disulfide bridge organization through ^1H NMR. This approach demonstrated that D-MCa is a mirror structure of L-MCa still displaying a significant basic face. D-MCa is a diastereomer rather than an enantiomer since only C_α are in the D-configuration. It is only for Thr^{26} and Ile^{28} that the side chain configurations differ from the exact mirror images. However, the different stereochemistry of the Thr and Ile side chains in D-MCa relative to the backbone did not cause any significant perturbations in the structure. Importantly enough, we observed that D-MCa was completely pharmacologically-inert indicating that the lock-and-key concept for the interaction of L-MCa with RyR is well preserved. Also, in spite of MCa's affinity for negatively-charged lipids of the plasma membrane (13), this finding also argues for a direct protein interaction of L-MCa with RyR in agreement with the cytoplasmic localization of MCa's binding site identified on RyR (12). Amazingly enough, D-MCa would therefore be the first example of a diastereomer toxin inactive on its pharmacological target. We also found that D-MCa keeps its ability to penetrate into cells, making this toxin the first known example of a folded/oxidized D-CPP. Since D-MCa appears to penetrate as well as L-MCa, but also presents cytoplasmic localization, a sign of membrane translocation, these data indicate that MCa / lipid interactions are conformation-insensitive. This was expected already from the finding that unfolded MCa, in which cysteine residues were replaced by 2-aminobutyric acid residues, also penetrated

efficiently in cells and also targeted associated cargoes to the cytoplasm (15). Besides cytoplasmic localization, both FAM-L-MCa and FAM-D-MCa also enter through endocytosis and end up into endosomal structures albeit to a lesser extent than with streptavidine as cargo instead of FAM. These findings argue also that endocytosis remains a major contributor of the cell entry of MCa. We conclude that D-MCa is a competitive pharmacologically-inert CPP that has the added advantage to be protease-resistant. It should also not be recognized by the immune system because likely resistant to proteolytic processing by T cells for presentation on major histocompatibility complexes. The maintained cell penetrating efficacy of this peptide should make it an ideal vector for *in vivo* applications.

REFERENCES

1. Lindgren, M., Hallbrink, M., Prochiantz, A., and Langel, U. (2000) *Trends Pharmacol Sci* **21**, 99-103
2. Zorko, M., and Langel, U. (2005) *Adv Drug Deliv Rev* **57**, 529-545
3. Pooga, M., Hallbrink, M., Zorko, M., and Langel, U. (1998) *Faseb J* **12**, 67-77
4. Derossi, D., Chassaing, G., and Prochiantz, A. (1998) *Trends Cell Biol* **8**, 84-87
5. Mae, M., and Langel, U. (2006) *Curr Opin Pharmacol* **6**, 509-514
6. Pooga, M., Soomets, U., Hallbrink, M., Valkna, A., Saar, K., Rezaei, K., Kahl, U., Hao, J. X., Xu, X. J., Wiesenfeld-Hallin, Z., Hokfelt, T., Bartfai, T., and Langel, U. (1998) *Nat Biotechnol* **16**, 857-861
7. Rhee, M., and Davis, P. (2006) *J Biol Chem* **281**, 1233-1240
8. Patel, L. N., Zaro, J. L., and Shen, W. C. (2007) *Pharm Res* **24**, 1977-1992
9. Oehlke, J., Scheller, A., Wiesner, B., Krause, E., Beyermann, M., Klauschenz, E., Melzig, M., and Bienert, M. (1998) *Biochim Biophys Acta* **1414**, 127-139
10. Fajloun, Z., Kharrat, R., Chen, L., Lecomte, C., Di Luccio, E., Bichet, D., El Ayeb, M., Rochat, H., Allen, P. D., Pessah, I. N., De Waard, M., and Sabatier, J. M. (2000) *FEBS Lett* **469**, 179-185
11. Esteve, E., Smida-Rezgui, S., Sarkozi, S., Szegedi, C., Regaya, I., Chen, L., Altafaj, X., Rochat, H., Allen, P., Pessah, I. N., Marty, I., Sabatier, J. M., Jona, I., De Waard, M., and Ronjat, M. (2003) *J Biol Chem* **278**, 37822-37831
12. Altafaj, X., Cheng, W., Esteve, E., Urbani, J., Grunwald, D., Sabatier, J. M., Coronado, R., De Waard, M., and Ronjat, M. (2005) *J Biol Chem* **280**, 4013-4016
13. Mabrouk, K., Ram, N., Boisseau, S., Strappazzon, F., Rehaim, A., Sadoul, R., Darbon, H., Ronjat, M., and De Waard, M. (2007) *Biochim Biophys Acta* **1768**, 2528-2540
14. Ram, N., Aroui, S., Jaumain, E., Bichraoui, H., Mabrouk, K., Ronjat, M., Lortat-Jacob, H., and De Waard, M. (2008) *J Biol Chem* **283**, 24274-24284
15. Ram, N., Weiss, N., Texier-Nogues, I., Aroui, S., Andreotti, N., Pirollet, F., Ronjat, M., Sabatier, J. M., Darbon, H., Jacquemond, V., and De Waard, M. (2008) *J Biol Chem*
16. Merrifield, R. B. (1969) *Adv Enzymol Relat Areas Mol Biol* **32**, 221-296
17. Hwang, T. L., Shaka, J. (1995) *Magn. Reson. Series A* **112**, 275-279
18. Marion, D., Ikuto, M., Tschudin, R., Bax, A. (1989) *J. Mag. Res.* **85**, 393-399
19. Marion, D., and Wuthrich, K. (1983) *Biochem Biophys Res Commun* **113**, 967-974
20. Delaglio, F., Grzesiek, S., Vuister, G. W., Zhu, G., Pfeifer, J., and Bax, A. (1995) *J Biomol NMR* **6**, 277-293
21. Wüthrich, K. (1986) *New york, John Wiley & Sons*, 2-199
22. Johnson, B. A., Blevins, R.A. (1994) *J. Biomol. NMR* **4**, 603-614
23. Herrmann, T., Guntert, P., and Wuthrich, K. (2002) *J Mol Biol* **319**, 209-227
24. Guntert, P., Mumenthaler, C., and Wuthrich, K. (1997) *J Mol Biol* **273**, 283-298
25. Vranken, W. F., Boucher, W., Stevens, T. J., Fogh, R. H., Pajon, A., Llinas, M., Ulrich, E. L., Markley, J. L., Ionides, J., and Laue, E. D. (2005) *Proteins* **59**, 687-696

26. Linge, J. P., Williams, M. A., Spronk, C. A., Bonvin, A. M., and Nilges, M. (2003) *Proteins* **50**, 496-506
27. Nabuurs, S. B., Nederveen, A. J., Vranken, W., Doreleijers, J. F., Bonvin, A. M., Vuister, G. W., Vriend, G., and Spronk, C. A. (2004) *Proteins* **55**, 483-486
28. Schwieters, C. D., Kuszewski, J. J., Tjandra, N., and Clore, G. M. (2003) *J Magn Reson* **160**, 65-73
29. Laskowski, R. A., Rullmannn, J. A., MacArthur, M. W., Kaptein, R., and Thornton, J. M. (1996) *J Biomol NMR* **8**, 477-486
30. Vriend, G. (1990) *J Mol Graph* **8**, 52-56, 29
31. Kim, D. H., Ohnishi, S. T., and Ikemoto, N. (1983) *J Biol Chem* **258**, 9662-9668
32. Mosbah, A., Kharrat, R., Fajloun, Z., Renisio, J. G., Blanc, E., Sabatier, J. M., El Ayeb, M., and Darbon, H. (2000) *Proteins* **40**, 436-442
33. Pallaghy, P. K., Nielsen, K. J., Craik, D. J., and Norton, R. S. (1994) *Protein Sci* **3**, 1833-1839
34. Lukacs, B., Sztretye, M., Almassy, J., Sarkozi, S., Dienes, B., Mabrouk, K., Simut, C., Szabo, L., Szentesi, P., De Waard, M., Ronjat, M., Jona, I., and Csernoch, L. (2008) *Biophys J* **95**, 3497-3509
35. Chen, L., Esteve, E., Sabatier, J. M., Ronjat, M., De Waard, M., Allen, P. D., and Pessah, I. N. (2003) *J Biol Chem* **278**, 16095-16106
36. Esteve, E., Mabrouk, K., Dupuis, A., Smida-Rezgui, S., Altafaj, X., Grunwald, D., Platel, J. C., Andreotti, N., Marty, I., Sabatier, J. M., Ronjat, M., and De Waard, M. (2005) *J Biol Chem* **280**, 12833-12839
37. Boisseau, S., Mabrouk, K., Ram, N., Garmy, N., Collin, V., Tadmouri, A., Mikati, M., Sabatier, J. M., Ronjat, M., Fantini, J., and De Waard, M. (2006) *Biochim Biophys Acta* **1758**, 308-319
38. Huang, F., and Du, W. (2009) *Toxicon* **54**, 153-160
39. Buczek, O., Yoshikami, D., Bulaj, G., Jimenez, E. C., and Olivera, B. M. (2005) *J Biol Chem* **280**, 4247-4253
40. Dutertre, S., Lumsden, N. G., Alewood, P. F., and Lewis, R. J. (2006) *FEBS Lett* **580**, 3860-3866
41. Buczek, O., Jimenez, E. C., Yoshikami, D., Imperial, J. S., Watkins, M., Morrison, A., and Olivera, B. M. (2008) *Toxicon* **51**, 218-229
42. di Luccio, E., Azulay, D. O., Regaya, I., Fajloun, Z., Sandoz, G., Mansuelle, P., Kharrat, R., Fathallah, M., Carrega, L., Esteve, E., Rochat, H., De Waard, M., and Sabatier, J. M. (2001) *Biochem J* **358**, 681-692
43. Beeton, C., Smith, B. J., Sabo, J. K., Crossley, G., Nugent, D., Khaytin, I., Chi, V., Chandy, K. G., Pennington, M. W., and Norton, R. S. (2008) *J Biol Chem* **283**, 988-997
44. Suchyna, T. M., Tape, S. E., Koeppe, R. E., 2nd, Andersen, O. S., Sachs, F., and Gottlieb, P. A. (2004) *Nature* **430**, 235-240

FOOTNOTES

This work was supported by grants from Technology pour la Santé (Program TIMOMA2 of the Commissariat à l'Energie Atomique) and from ANR PNANO (Programs SYNERGIE and NanoFret). Hicham Bichraoui and Michel Ronjat are supported by a grant of Association Française contre les Myopathies. We thank Cédric Bernard for help in solving D-MCa structure and Eric Denarier for image analysis. Mass spectrometry analyses were performed by the Centre d'Investigation Clinique of Grenoble under the heading of Dr. Michel Sève.

The abbreviations used are: CD: Circular Dichroism; CPP: Cell Penetrating Peptide; DMF: dimethyformamide; FACS: Fluorescence-Activated Cell Sorting; FAM: 5(6)-carboxyfluorescein; ^{1}H-NMR: proton nuclear magnetic resonance; HPLC: high-performance liquid chromatography; MCa:

Maurocalcine; NMP: N-methyl-pyrrolidone; nOe: nuclear Overhauser effect; rmsd: root mean square deviation; RS: Sarcoplasmic reticulum; RyR: Ryanodine Receptor; TFA: trifluoroacetic acid.

FIGURE LEGENDS

Fig. 1. Chemical synthesis and enzymatic resistance of D-MCa. (A) Amino acid sequence of D-MCa in single letter code. The positions of half-cystine residues are highlighted. The disulfide bridge organization of D-MCa, as expected from the connectivity of L-MCa, is illustrated by red lines. (B) Analytical C_{18} reversed-phase HPLC profile of D-MCa at different stages of its chemical synthesis (black line: crude reduced peptide after final TFA treatment; red line: purified D-MCa 72 hrs after folding and oxidation as witnessed by the shift in elution time). Inserts: mass spectra of reduced (black line, right) and oxidized (red line, left) D-MCa. (C) Analytical C_{18} reversed-phase HPLC profiles illustrating the resistance of D-MCa to proteolysis by 36 hrs trypsin or endoproteinase Asp-N treatments (upper panels). In identical experimental conditions, these enzymes efficiently degrade L-MCa (lower panels).

Fig. 2. Determination of the secondary structure of D-MCa by circular dichroism and thermal stability. (A) CD spectra of D-MCa *versus* L-MCa. (B) CD spectra of D-MCa measured at various temperatures (from 20°C up to 100°C). (C) Ellipticity of D-MCa at 200 nm measured as a function of temperature.

Fig. 3. ^{1}H-NMR 3-D structure of D-MCa in solution. (A) Left: plot of the number of intra-residue (black), sequential (medium grey), medium (dark grey) and long range (light grey) nOe. The restraints were classified by the Wüthrich's method. Right: local value of rmsd (in Å) calculated on backbone atoms in black and in grey on all heavy atoms except hydrogen. Arrows denote β strands. (B) 20 best D-MCa and L-MCa structures (only backbone atoms are displayed) superimposed for best fit. β strands are depicted in blue. N-ter and C-ter correspond to N- and C-terminal extremities. (C) Ribbon drawing of the averaged D-MCa structure, compared to L-MCa structure. The β strands, Cα backbone traces and disulfide bridges are shown in blue, green and grey, respectively. The disulfide bridges are represented in ball and sticks. The six half-cystine residues are numbered according to their positions in MCa amino acid sequence.

Fig. 4. Superimposition of L-MCa (in blue) with D-MCa drawn in the L-configuration (yellow). To achieve this inversion, the PDB file of D-MCa was modified. Lateral chains of seven Lys and four Arg residues are also shown.

Fig. 5. D-MCa lacks pharmacological activity. (A) [^{3}H]-ryanodine binding on heavy SR vesicles was measured in the presence of various concentrations of L-MCa (black filled symbols) or D-MCa (red filled symbols). [^{3}H]-ryanodine binding was measured at pCa 5 in the presence of 10 nM [^{3}H]-ryanodine for 2.5 hrs at 37°C. Non specific binding was constant at all MCa concentrations and in all cases represented less than 8% of total binding. Data for L-MCa were fitted with a sigmoid function $y = y_0 + (a / (1 + x^b/c^b))$, where $y_0 = 0.06$ at MCa = 0 nM, $a = 6.2$ is the maximal binding stimulation factor over basal value, $b = -1$ the slope coefficient, and $c = 17.8$ nM is the EC_{50} for L-MCa effect. D-MCa is without effect on [^{3}H]-ryanodine binding. (B) Effect of D-MCa and L-MCa on Ca^{2+} release from heavy SR vesicles. Heavy SR vesicles were actively loaded with Ca^{2+} by five sequential additions of 2 μM Ca^{2+} in the monitoring chamber. Addition of 1 μM D-MCa has no effect on Ca^{2+} release, whereas a subsequent application of 60 nM L-MCa produces a massive sustained Ca^{2+} release. Application of 0.5 mM EGTA chelates the released Ca^{2+} and lowers the absorbance.

Fig. 6. D-MCa is comparable to L-MCa for cell penetration. (A) Primary structure of FAM-D-MCa. 5(6)-carboxyfluorescein was coupled to D-MCa by a peptidic bond at the N-terminus of the peptide. (B) Analytical C_{18} reversed-phase HPLC profile of folded/oxidized D-MCa (black line) and of folded/oxidized FAM-D-MCa (green line). The rightward shift of the elution time for FAM-D-MCa is due to the hydrophobicity of FAM. The peak comes out as a doublet because of the presence of two

isomers of FAM. (C) Confocal microscopy images comparing cell penetration of FAM-D-MCa with that of FAM-L-MCa (green labeling). Plasma membranes are labeled with concanavalin-A-rhodamin (in red). White arrows denote diffuse cytoplasmic and nuclear distribution of FAM-D-MCa and FAM-L-MCa, while yellow arrows illustrate a predominant punctuate distribution of the peptides. CHO cells were incubated 2 hrs with 10 μM peptide concentration. (D) Average number of colored pixel per image for plasma membrane and FAM-D-MCa staining. Average number of bi-colored pixels is also provided. N=3 experiments, pixel quantification on 20 visual fields (x40 objective), average labeled pixels for 10 visual fields on one representative experiment. NS, non significant, **, $p \leq 0.01$.

Fig. 7. Mode of cell penetration of FAM-D-MCa. (A) Confocal microscopy image of CHO cells showing the intracellular distribution of FAM-D-MCa (in green) and LysoTracker red DND-99 (in blue, pseudo color). Experimental conditions: cells were incubated 2 hrs with 1 μM FAM-D-MCa and 20 min with 50 nM LysoTracker red DND-99 before confocal acquisition. (B) Average number of colored pixel per image for LysoTracker red DND-99 and FAM-D-MCa staining. Average number of bi-colored pixels is also provided. N=3 experiments, pixel quantification on 14 visual fields (x40 objective), average labeled pixels for 10 visual fields on one representative experiment. **, $p \leq 0.001$. (C) Representative example of FACS histograms for FAM-D-MCa cell penetration in the absence of any drug or in the presence of 1 mM amiloride, 5 μM cytochalasin D, 5 mM nocodazole, or 5 mM methyl-β-cyclodextrin. All these drugs were also preincubated 30 min with CHO cells before addition of 1 μM FAM-D-MCa. (D) Average inhibition of FAM-D-MCa cell penetration by endocytosis-inhibiting drugs as calculated from FACS experiments. N=3 experiments, *, $p \leq 0.05$, **, $p \leq 0.01$, and ***, $p \leq 0.001$.

Fig. 8. Dose-dependent cell penetration of FAM-D-MCa and FAM-L-MCa and lack of cell toxicity. (A) FACS histograms for each FAM-D-MCa concentration. Cell penetration time was 2 hrs and cells were gated immediately after cell detachment by trypsin treatment. 50,000 events were gated by FACS for each concentration. (B) FACS histograms for FAM-L-MCa performed in similar conditions than for FAM-D-MCa. (C) Mean cell fluorescence as a function of FAM-D-MCa (open symbols) or FAM-L-MCa (filled symbols) concentration. Data were fitted with a sigmoid function $y=a/(1+\exp(-(x/x_0)/b))$ where a = 187 (FAM-D-MCa) or 175 (FAM-L-MCa) maximal arbitrary fluorescence units, x_0=1384 nM (FAM-D-MCa) or 1783 nM (FAM-L-MCa) the concentration of half-maximal cell penetration, and b=417 (FAM-D-MCa) or 576 (FAM-L-MCa). (D) Cell viability as assessed by the MTT test. 0.1% saponin, 10 μM L-MCa or 10 μM D-MCa were incubated for 24 hrs with CHO cells in culture. N=3 experiments, triplicates, NS, non significant, ***, $p \leq 0.001$.

Table 1: Resonance assignment of D-MCa.

Table 2: Structural statistics of the 20 best D-MCa structures.

Figure 1

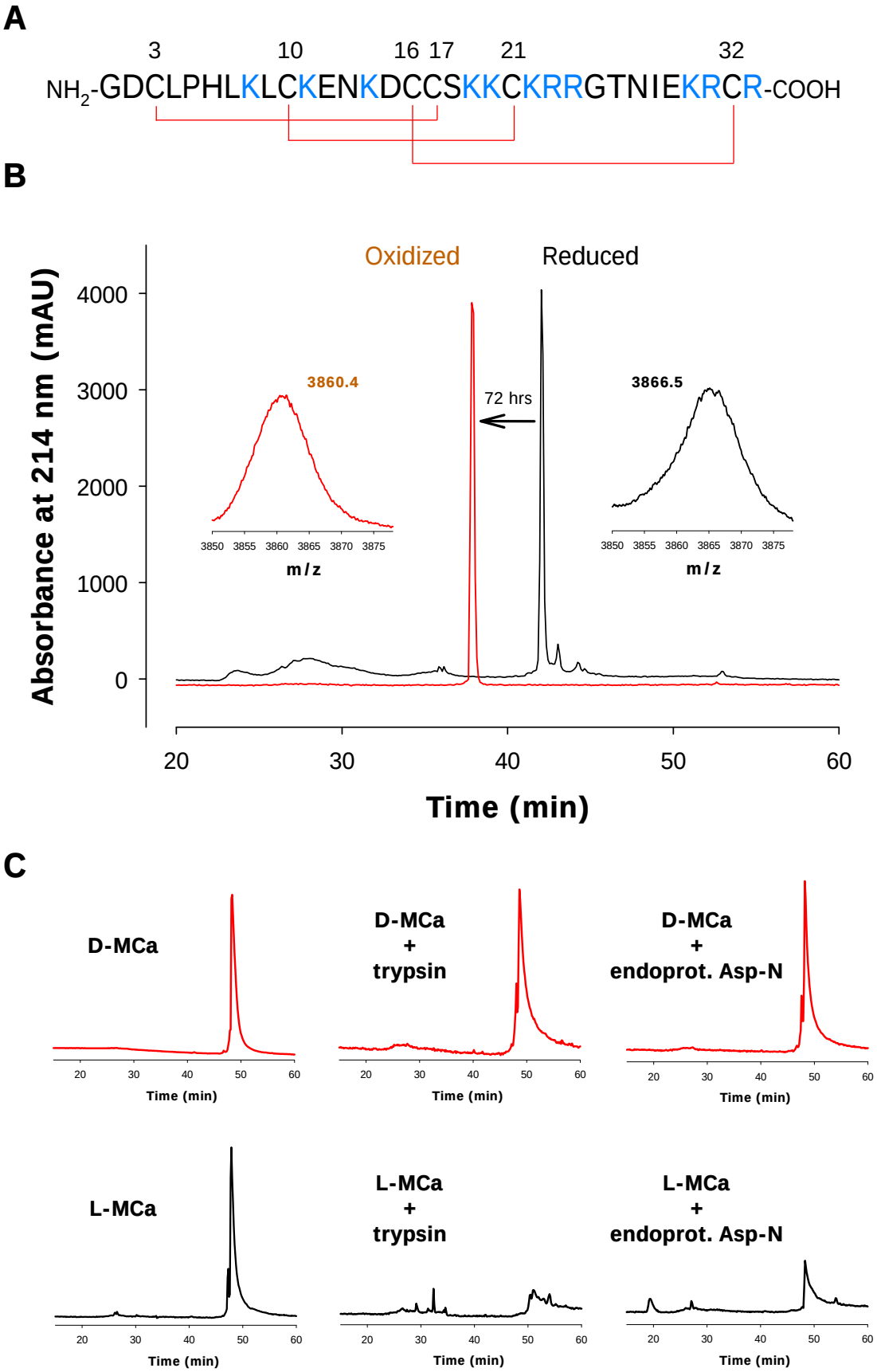
A
3
10
16 17
21
32
NH2-GDCLPHLKLCKENKDCCSKKCKRRGTNIEKRCR-COOH
B
Oxidized
Reduced
Absorbance at 214 nm (mAU)
4000
3000
2000
1000
0
3860.4
72 hrs
3866.5
3850 3855 3860 3865 3870 3875
m/z
3850 3855 3860 3865 3870 3875
m/z
20
30
40
50
60
Time (min)
C
D-MCa
D-MCa + trypsin
D-MCa + endoprot. Asp-N
L-MCa
L-MCa + trypsin
L-MCa + endoprot. Asp-N
20 30 40 50 60
Time (min)

Figure 2

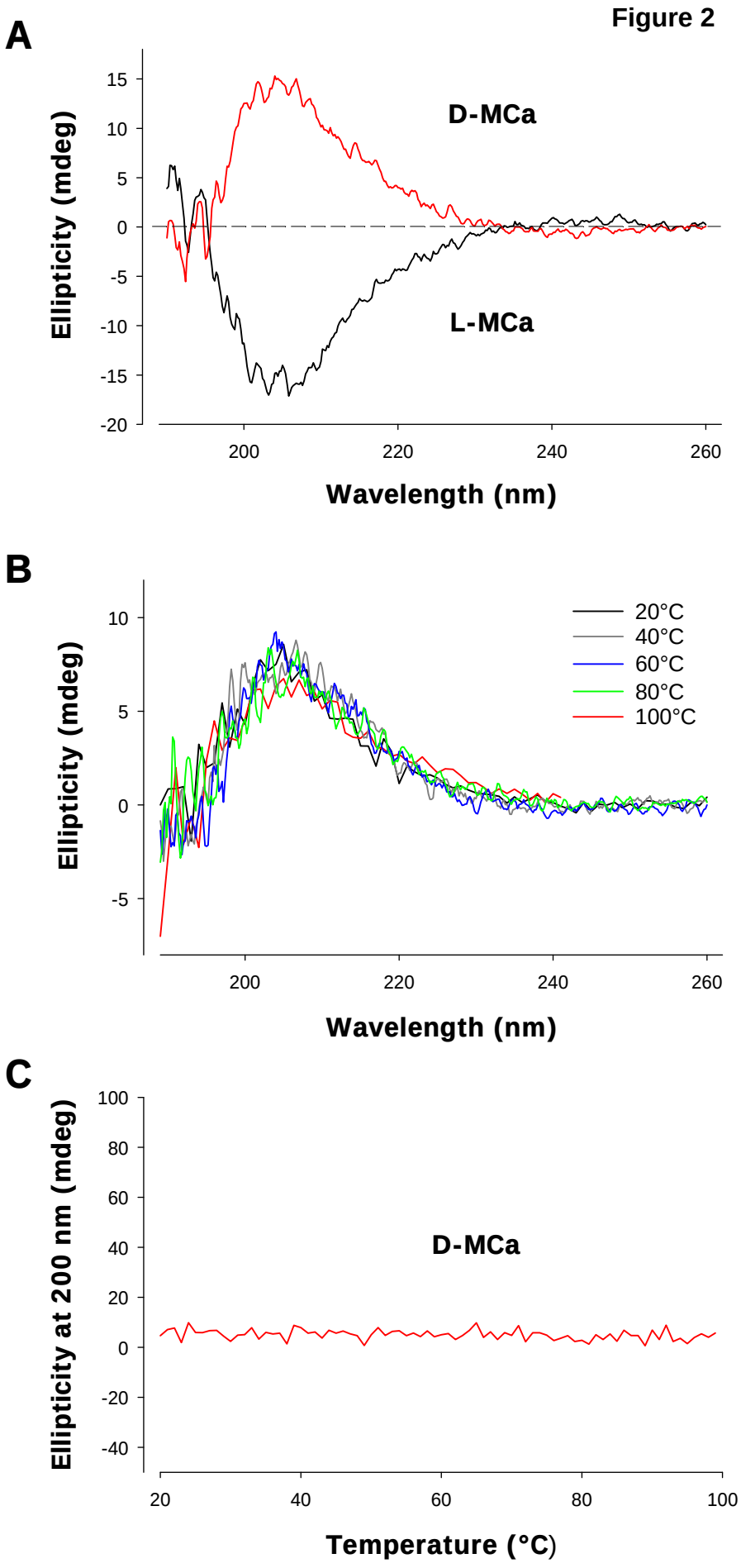
A
Ellipticity (mdeg)
15
10
5
0
-5
-10
-15
-20
D-MCa
L-MCa
200
220
240
260
Wavelength (nm)
B
Ellipticity (mdeg)
10
5
0
-5
20°C
40°C
60°C
80°C
100°C
200
220
240
260
Wavelength (nm)
C
Ellipticity at 200 nm (mdeg)
100
80
60
40
20
0
-20
-40
D-MCa
20
40
60
80
100
Temperature (°C)

Figure 3

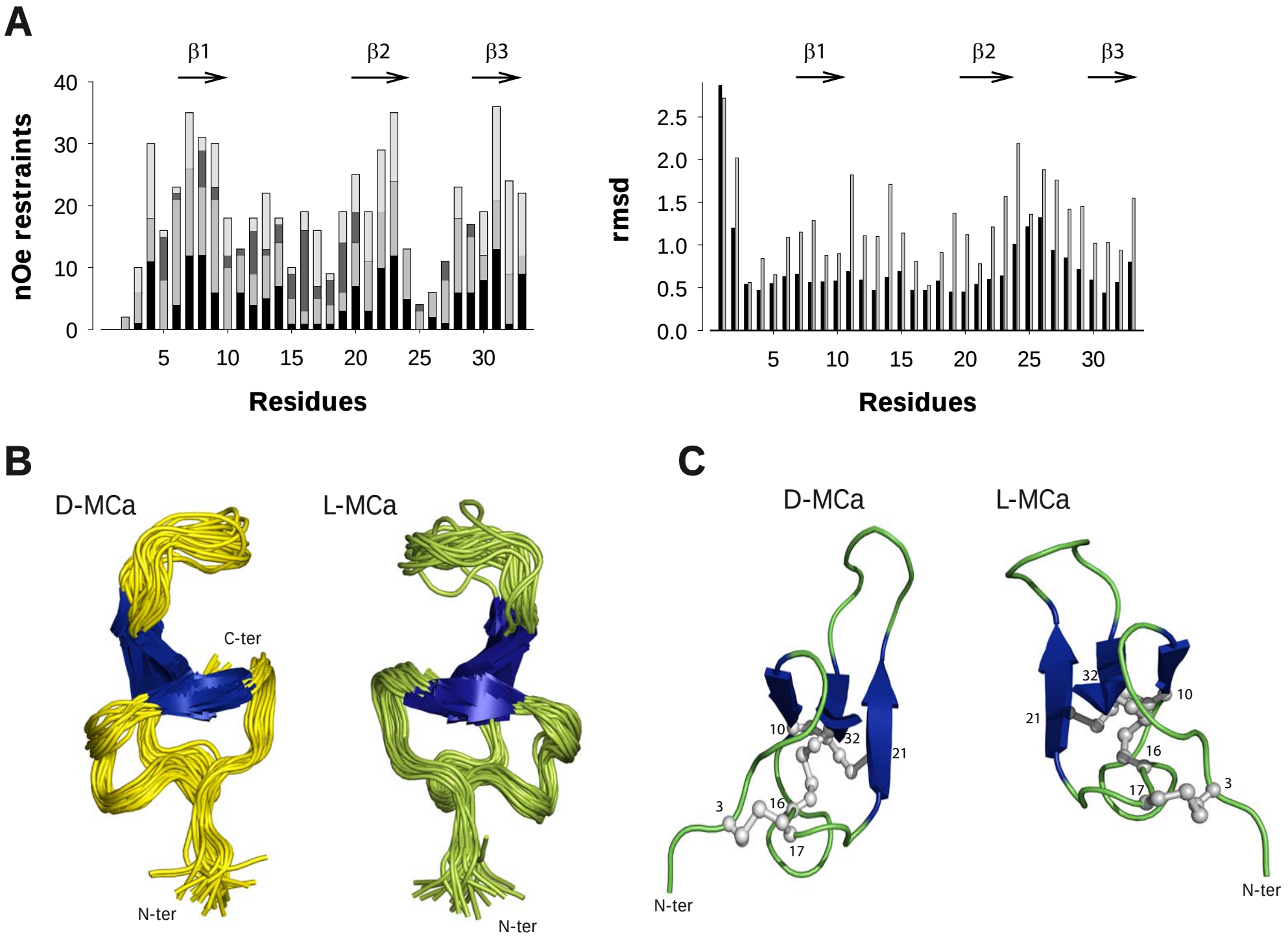
A
β1
β2
β3
nOe restraints
40
30
20
10
0
5
10
15
20
25
30
Residues
rmsd
2.5
2.0
1.5
1.0
0.5
0.0
B
D-MCa
L-MCa
C-ter
N-ter
N-ter
C
D-MCa
L-MCa
10
32
21
3
16
17
N-ter
32
10
21
16
17
3
N-ter

Figure 4

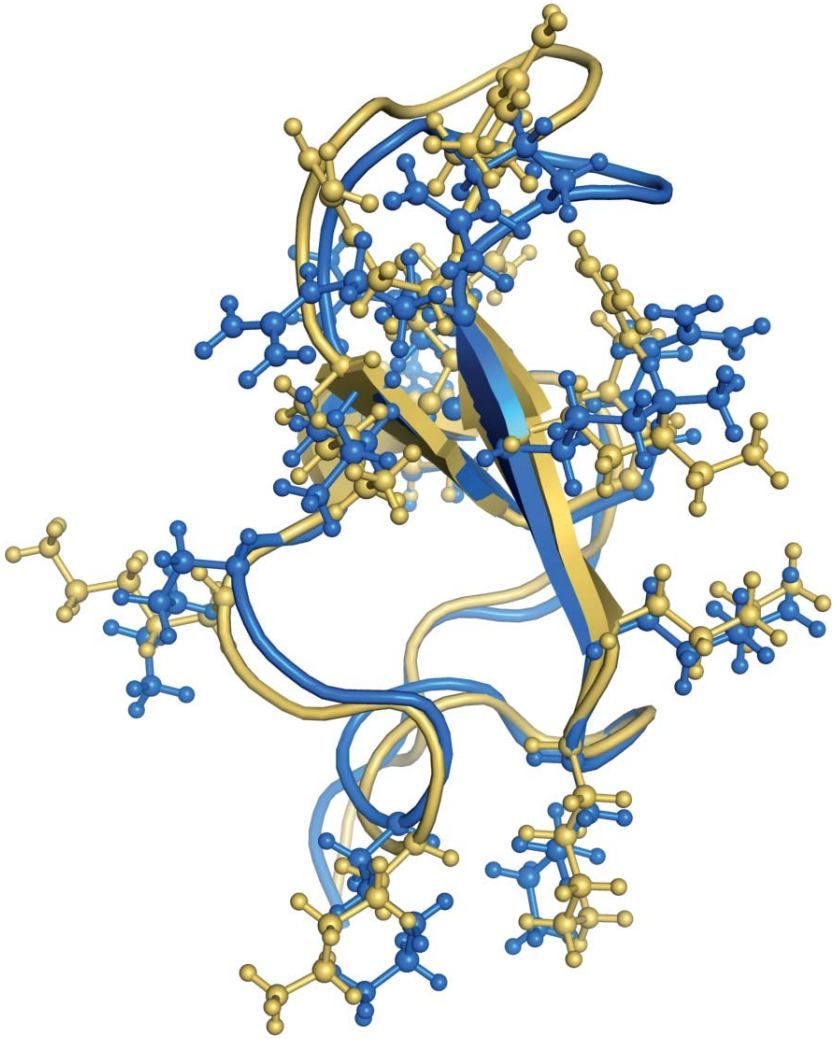

Figure 5

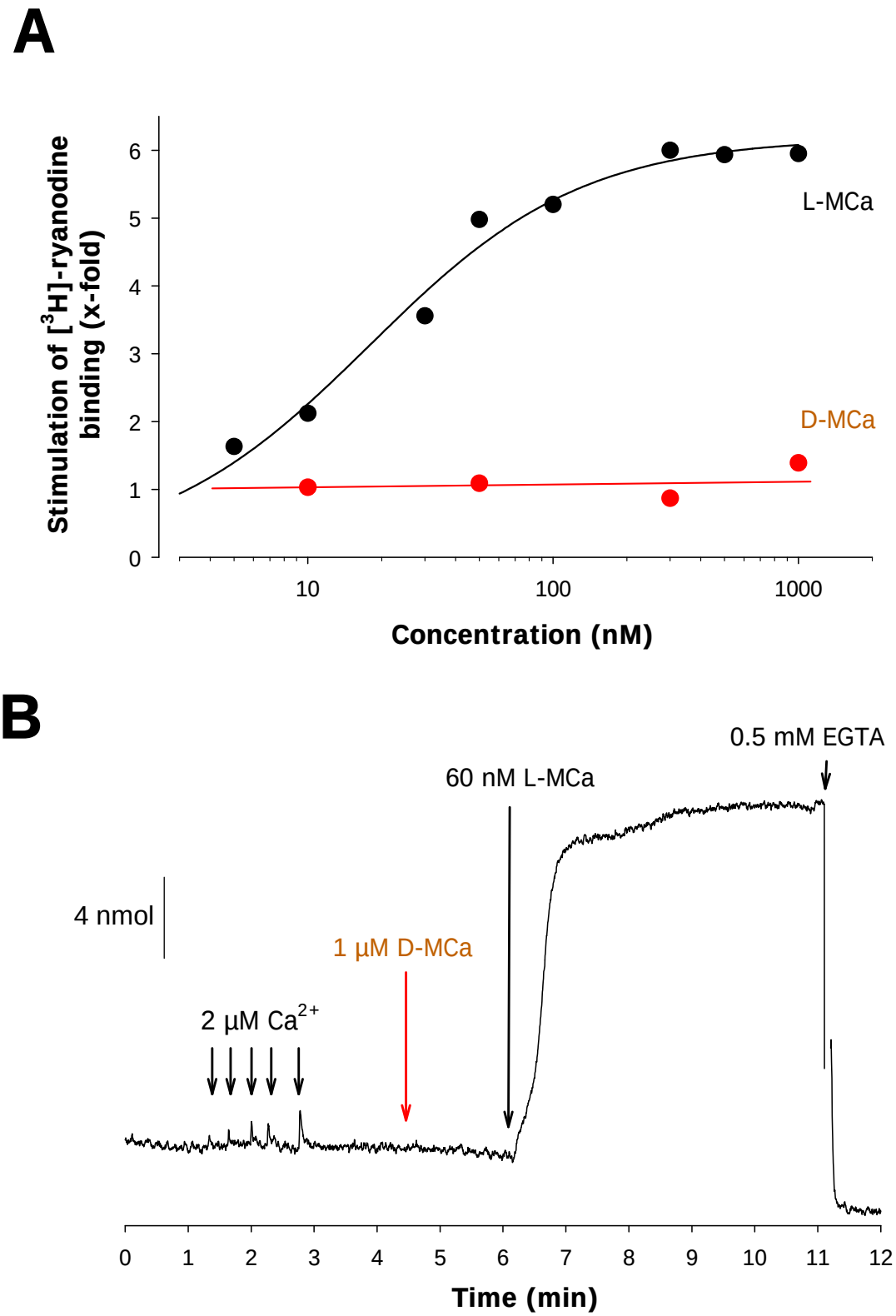
A
Stimulation of [3H]-ryanodine binding (x-fold)
0
1
2
3
4
5
6
10
100
1000
Concentration (nM)
L-MCa
D-MCa
B
0.5 mM EGTA
60 nM L-MCa
4 nmol
1 µM D-MCa
2 µM Ca2+
0
1
2
3
4
5
6
7
8
9
10
11
12
Time (min)

Figure 6

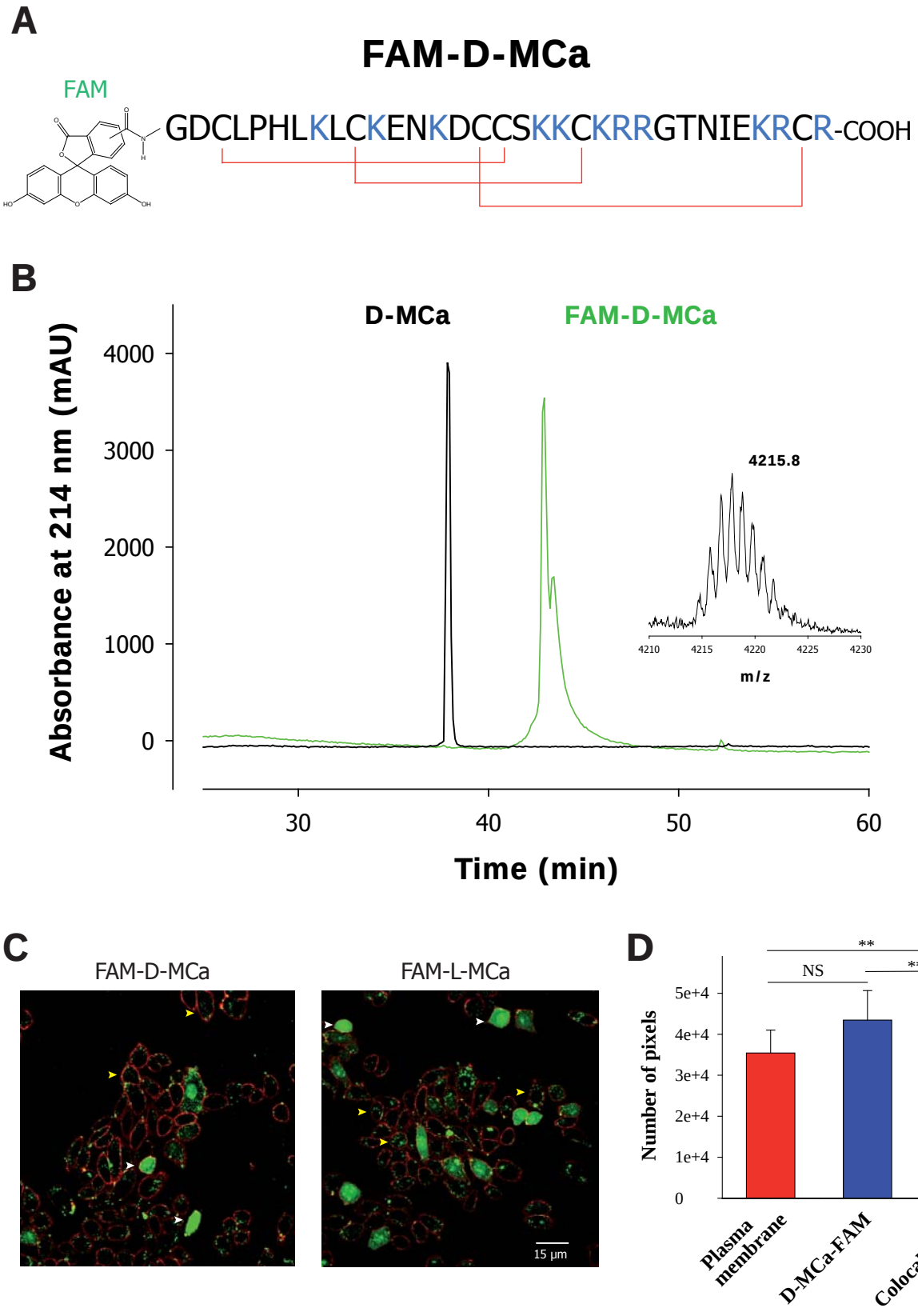
A
FAM-D-MCa
FAM
GDCLPHLKLCKENKDCCSKKCKRRGTNIEKRCR-COOH
B
D-MCa
FAM-D-MCa
Absorbance at 214 nm (mAU)
4000
3000
2000
1000
0
30
40
50
60
Time (min)
4215.8
4210
4215
4220
4225
4230
m/z
C
FAM-D-MCa
FAM-L-MCa
15 µm
D
**
NS
**
Number of pixels
5e+4
4e+4
3e+4
2e+4
1e+4
0
Plasma membrane
D-MCa-FAM
Colocalization

Figure 7

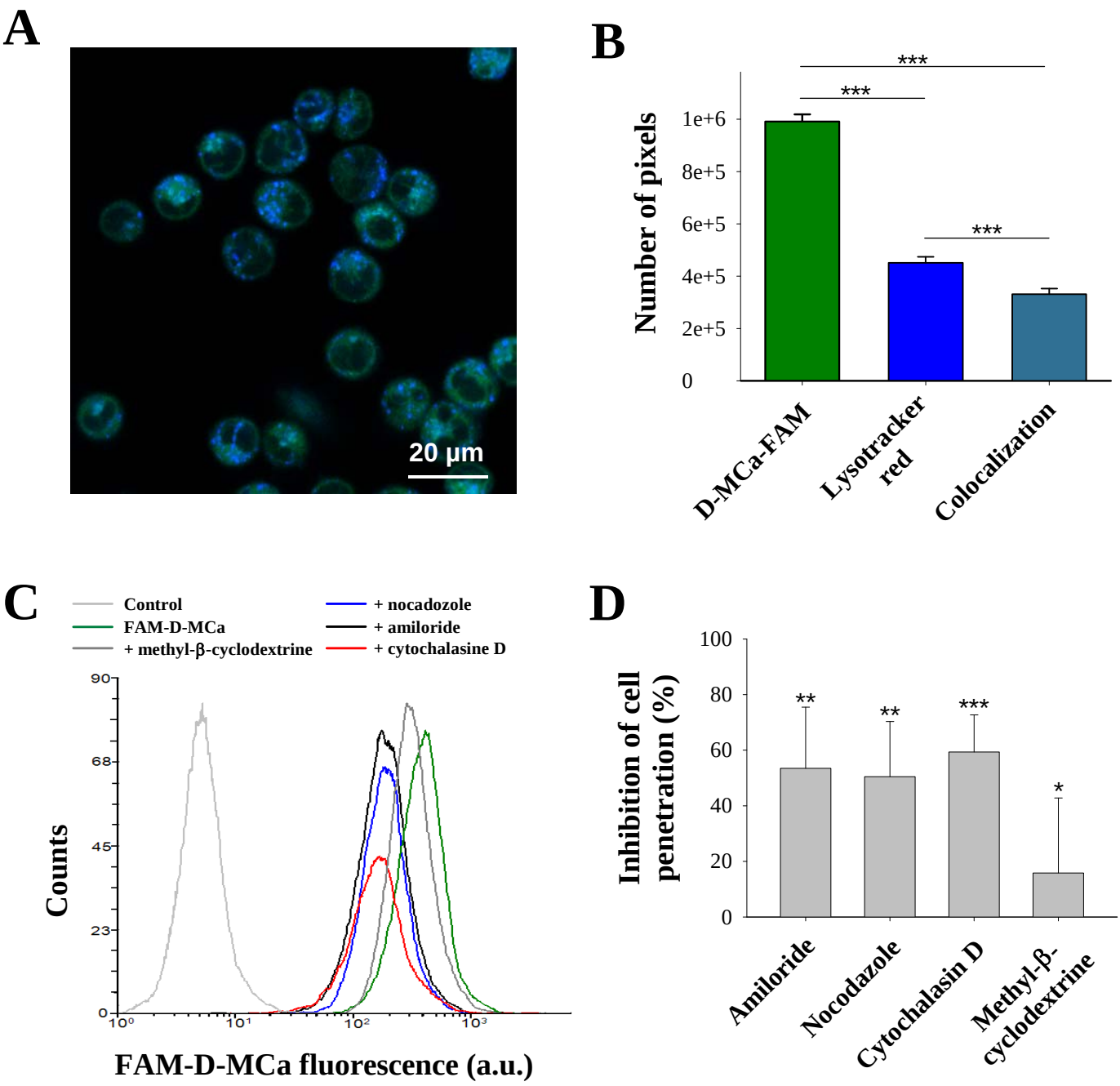
A
20 µm
B
Number of pixels
1e+6
8e+5
6e+5
4e+5
2e+5
0
***
***
***
D-MCa-FAM
Lysotracker red
Colocalization
C
Control
FAM-D-MCa
+ methyl-β-cyclodextrine
+ nocadozole
+ amiloride
+ cytochalasine D
Counts
90
68
45
23
0
10⁰
10¹
10²
10³
FAM-D-MCa fluorescence (a.u.)
D
Inhibition of cell penetration (%)
100
80
60
40
20
0
**
**
***
*
Amiloride
Nocodazole
Cytochalasin D
Methyl-β-cyclodextrine

Figure 8

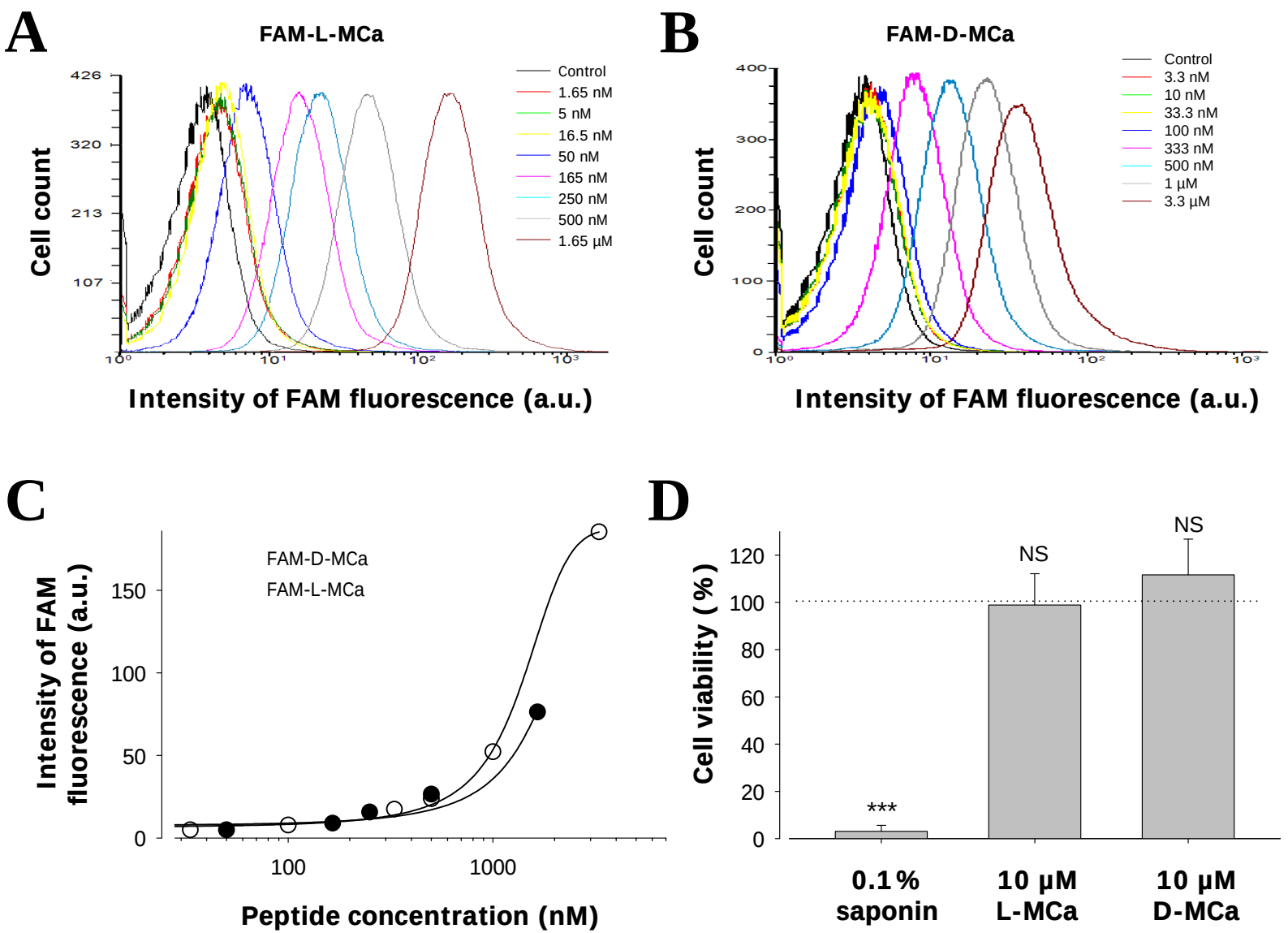
A
FAM-L-MCa
Cell count
426
320
213
107
Control
1.65 nM
5 nM
16.5 nM
50 nM
165 nM
250 nM
500 nM
1.65 µM
Intensity of FAM fluorescence (a.u.)
B
FAM-D-MCa
Cell count
400
300
200
100
0
Control
3.3 nM
10 nM
33.3 nM
100 nM
333 nM
500 nM
1 µM
3.3 µM
Intensity of FAM fluorescence (a.u.)
C
Intensity of FAM fluorescence (a.u.)
150
100
50
0
FAM-D-MCa
FAM-L-MCa
100
1000
Peptide concentration (nM)
D
Cell viability (%)
120
100
80
60
40
20
0
NS
NS
***
0.1% saponin
10 µM L-MCa
10 µM D-MCa

Table 1: Resonance assignment of D-MCa. * represent resonance that cannot be observed. Chemical shifts are given in ppm.

Residue	HN	HC^{α}	HC^{β}	Other
G^{1}		3.78, *		
D^{2}	8.69	4.74	2.72, 2.82	
C^{3}	8.17	4.65	2.82, 3.09	
L^{4}	9.11	4.72	2.1, *	HC^{γ}: 1.78; $HC^{\delta1}$: 0.86; $HC^{\delta2}$: 1.24
P^{5}		4.48	2.12, 2.26	HC^{γ}: 1.72, 2.06; $HC^{\delta1}$: 3.53; $HC^{\delta2}$: 3.94
H^{6}	8.01	4.07	2.98, 3.13	2H: 7.3; 4H: 8.62
L^{7}	9.27	3.45	1.48, 1.86	HC^{γ}: 0.23; $HC^{\delta1}$: 0.52; $HC^{\delta2}$: 0.62, *
K^{8}	7.36	4.21	1.71, 1.8	$HC^{\gamma1}$: 1.34; $HC^{\gamma2}$: 1.45; HC^{δ}: 1.62, *; $HC^{\varepsilon1}$: 2.83; $HC^{\varepsilon2}$: 2.94; HN^{ζ}: *
L^{9}	8.15	4.5	1.36, 1.51	HC^{γ}: 1.59; $HC^{\delta1}$: 0.75; $HC^{\delta2}$: 0.84, *
C^{10}	7.88	4.81	2.95, 3.02	
K^{11}	8.6	4.31	1.53, 1.76	HC^{γ}: 1.25, *; HC^{δ}: 2.89; HC^{ε}: *; HN^{ζ}: *
E^{12}	7.74	4.58	1.75	HC^{γ}: 2.21
N^{13}	8.96	3.87	2.72	NH2: 6.76, 7.64
K^{14}	8.36	3.93	1.72, 1.83	HC^{γ}: 1.21, *; HC^{δ}: 1.21, *; HC^{ε}: 2.83, *; HN^{ζ}: *
D^{15}	7.67	4.31	2.89	
C^{16}	7.68	4.88	2.5, 3.39	
C^{17}	9.98	4.4	2.75, 3.11	
S^{18}	9.22	4.1	3.76, 3.98	
K^{19}	7.52	4.06	1.84, 2	$HC^{\gamma1}$: 1.17; $HC^{\gamma2}$: 1.28; $HC^{\delta1}$: 1.46; $HC^{\delta2}$:1.71; HC^{ε}: 2.91; HN^{ζ}: *
K^{20}	7.3	4.31	1.58	$HC^{\gamma1}$: 1.11; $HC^{\gamma2}$: 1.27; HC^{δ}: 1.42, *; HC^{ε}: 2.85, *; HN^{ζ}: *
C^{21}	8.88	4.84	2.6, 2.85	
K^{22}	8.24	4.85	1.51, 1.87	HC^{γ}: 1.25; HC^{δ}: 1.61; HC^{ε}: 2.88, *; HN^{ζ}: *
R^{23}	9	4.52	1.49, 1.63	HC^{γ}: 1.38, *; HC^{δ}: 3.07, *; HN^{ε}: 6.74
R^{24}	8.79	4.38	1.63, 1.67	HC^{γ}: 1.44, *; HC^{δ}: 3.04, *; HN^{ε}: 7.13
G^{25}	8.65	3.7, 4		
T^{26}	8.42	4.06	4.3	HC^{γ}: 1.09
N^{27}	7.9	4.56	2.89	NH2: 6.88, 7.59
I^{28}	8.24	3.87	1.87	$HC^{\gamma1}$: 1.18; $HC^{\gamma2}$: 1.26; $HC^{\gamma3}$: 0.87; HC^{δ}: 0.76
E^{29}	8.11	4.08	1.73, 1.85	HC^{γ}: 2.3
K^{30}	8.39	3.92	1.74	HC^{γ}: 0.96, *; HC^{δ}: 1.47, *; HC^{ε}: 2.77, *; HN^{ζ}: *
R^{31}	7.59	5.14	1.04, 1.12	HC^{γ}: 1.23; $HC^{\delta1}$: 2.76; $HC^{\delta2}$: 3.01; HN^{ε}: 7.2
C^{32}	8.52	5.17	2.86, 3.26	
R^{33}	9.05	4.33	1.75, 2	$HC^{\gamma1}$: 1.55; $HC^{\gamma2}$: 1.62; $HC^{\delta1}$: 2.84; $HC^{\delta2}$: 2.98; HN^{ε}: 6.63

Table 2: Structural statistics of the 20 best D-MCa structures. [a] No NOE restraint was violated by more than 0.1 Å. [b] Residues involved in secondary structure elements : 8-10, 20-23, and 30-32. [c] Values based on Whatif analysis.

Restraints information[a]	
NOE derived distance restraints	390
Intra-residual (i, i)	158
Sequential (i, i+1)	116
Medium range (2<|i-j|<4)	36
Long range (|i-j|>5)	80
Hydrogen bonds	12
Pairewise cartesian r.m.s.d. (Å)	
Backbone atoms[b] (C, Cα, N)	0.41 ± 0.09
All heavy atoms[b]	1.33 ± 0.22
Average r.m.s. Z-scores deviation from current reliable structures[c]	
Bond lengths	0.76 ± 0.05
Bond angles	0.83 ± 0.05
Average r.m.s.d. from experimental restraints	
Distance restraints (Å)	$9.5 \times 10^{-3} \pm 0.3 \times 10^{-3}$
Energies (kcal.M^{-1})	
Total	-176.074
NOE	2.06
Ramachandran quality paramaters (%)	
Favored regions	73.8
Allowed regions	21.90
Additionally allowed regions	3.80
Disallowed regions	0.5